Supplementary Information for

Specific Ion Selectivity in Sulfonated Polystyrene Membranes Near the Percolation Threshold

Yuxuan Huang,†,1 Marshall C. Tekell,†,2 Jingchao Qin,2 Sanat K. Kumar,*,2 and Ngai Yin Yip*,1,3

[1]Department of Earth and Environmental Engineering, Columbia University, New York, New York 10027
[2]Department of Chemical Engineering, Columbia University, New York, New York 10027
[3]Columbia Water Center, Columbia University, New York, New York 10027

†Equal contributions

Corresponding Authors
*Sanat K. Kumar − Department of Chemical Engineering, Columbia University, New York, New York 10027-6623, United States; Phone: +1 (212) 854-2193; Email: sk2794@columbia.edu;
Ngai Yin Yip − Department of Earth and Environmental Engineering and Columbia Water Center, Columbia University, New York, New York 10027-6623, United States; orcid.org/0000-0002-1986-4189; Phone: +1 (212) 854-2984; Email: n.y.yip@columbia.edu

Table of Contents

MATERIALS AND METHODS

Section S1: Determination of sulfonation level

As described in the Materials and Methods Section of the main manuscript, copolymers were dissolved in Acetone-D_6 and characterized using ^{1}H-NMR. Gaussian curves were fitted to each of the three peaks (Figure S1). The areas underneath the peaks (a, b, c) were analyzed and used to calculate $SL = (c/2)/(c/2+b/2)$, as indicated in the inset.

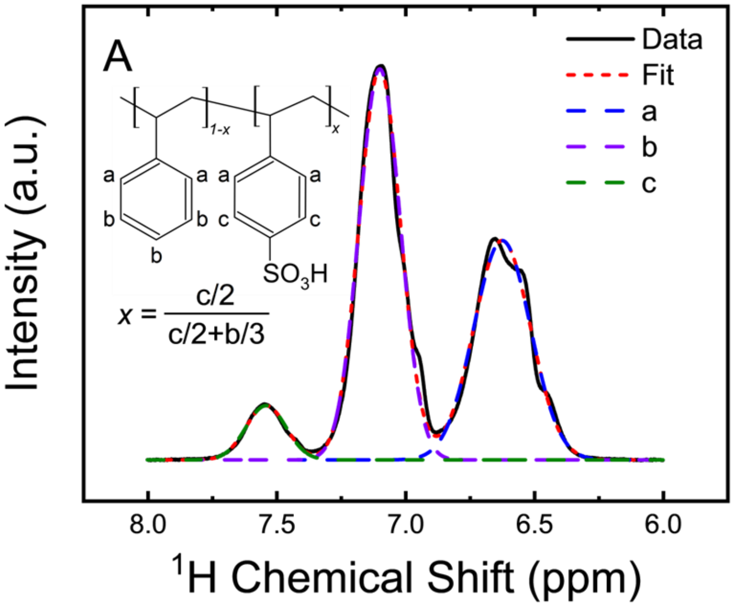

Figure S1: Example ^{1}H-NMR spectrum used to determine the sulfonation level, *SL*, of PS-r-SPSH statistical copolymers.

Section S2: Analysis of membrane surface morphology and thickness correction

The morphology of fabricated PS-r-SPS membranes was probed by scanning electron microscope (SEM, Zeiss Sigma VP, Oberkochen, Germany). Hydrated membranes were frozen in liquid nitrogen and then cut with a blade to expose the cross sections. Samples were mounted onto specimen holders with carbon tapes, with ≈10 nm Au coating applied (108 auto sputter, Cressington, UK) before imaging. The cross-sectional micrographs reveal that one surface of the membranes shows a wavy pattern of non-uniform thickness, with one representative repeating pattern exhibited in Figure S2A. The irregular thickness is due to the uneven surface of the custom-made polytetrafluoroethylene (PTFE) mold used for solvent evaporation during membrane fabrication. Further analysis of the SEM micrographs indicates that variations within crest thickness and within trough thickness are relatively small between the repeating wavy microstructures. Membrane thickness at the crest of the wavy microstructure, averaged from SEM micrographs, is in close agreement with the value characterized by a digital micrometer (difference <10%). Because of the unevenness, the membrane thickness measured with the digital micrometer cannot properly represent the effective thickness for ion transport during ionic conductivity characterizations.

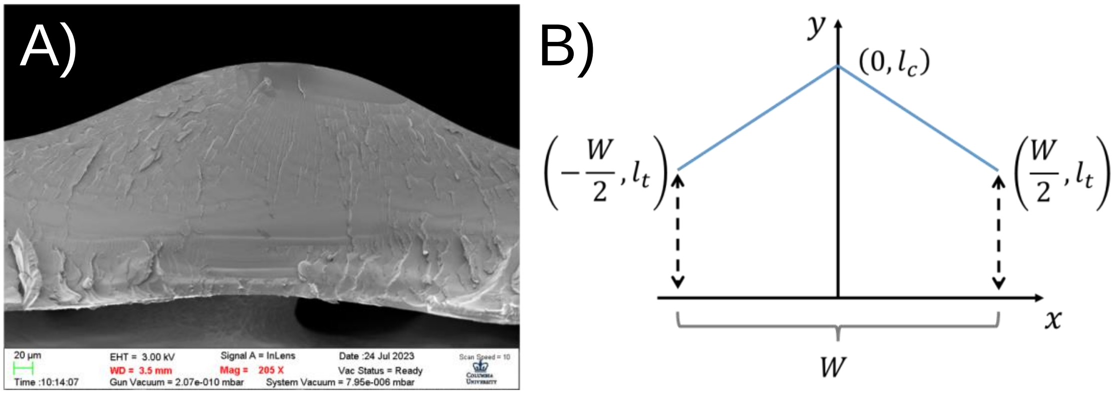

Figure S2: A) A representative cross-sectional view of SEM micrographs of the fabricated PS-r-SPS membranes. B) Schematic illustrating the approximation of effective membrane thickness, where l_c, l_t, and W denote the crest thickness, trough thickness, and width, respectively, of the repeating unit of wavy microstructure.

To approximate a relation between the effective membrane thickness and the crest thickness, the repeating unit of wavy microstructure displayed in Figure S2A is simplified as the schematic in Figure S2B. Here, l_c, l_t, and W are the crest thickness, trough thickness, and width, respectively, of the repeating microstructure unit. Assuming the resistivity of the membrane material to be ρ, the resistance of a repeating unit, R, can be calculated as[1]

$$R = \frac{\rho}{\int_{-W/2}^{W/2} \frac{dx}{y(x)}} \tag{S1}$$

where $y(x)$ is the membrane thickness at coordinate x. For a rectangular prism resistor with the same ρ and W but a thickness of l_e, the resistance R_e is

$$R_e = \frac{\rho l_e}{W} \tag{S2}$$

Equating R and R_e in Eqs. S1 and S2, respectively, and solving for l_e gives the effective thickness of the fabricated membrane.

Cross-sectional SEM micrographs of 10 locations of a fabricated membrane were analyzed for average values of l_c, l_t, and W. The ratio of the effective thickness to the crest thickness, l_e/l_c, is the correction factor relating the thickness measured by digital micrometer to the effective thickness of the membrane. l_e/l_c is determined to be 0.857. As the crest thickness and trough thickness each have a relatively small coefficient of variation (< 8.8%), the correction factor can be applied to all fabricated membranes with reasonable accuracy. Multiplying the digital micrometer thickness by the correction factor yields the effective membrane thickness, which is used in Eq. 5 of the main manuscript to determine the membrane ionic conductivity.

Section S3: Characterization of ion transport selectivity

A 3D-printed four-chamber cell was used to characterize the selective transport between different counterions through the IEM under an applied electric field (Figure S3A). Figure 3B shows a schematic of the electrodialysis setup for a representative experiment to determine selectivity between Li^+ and K^+. The feed chamber (3) and receiver chamber (2) are separated by the cation exchange membrane, CEM, to be evaluated and abutted by two anion exchange membranes, AEMs (Selemion AMV). The feed chamber contains 5.0 mL of 0.050 eq L^{-1} LiCl and 0.050 eq L^{-1} KCl solution, whereas the receiver chamber has 5.0 mL of NH_4Cl solution at the same total concentration as the feed solution. The setup is bookended by chambers (1) and (4), each with a Pt-coated Ti mesh as a working or counter electrode. The cation of the nitrate solutions in chambers (1) and (4) is purposefully selected to prevent interference with the measurement of target ion concentrations in chamber (2), e.g., Na^+ for Li^+/K^+ selectivity characterizations.

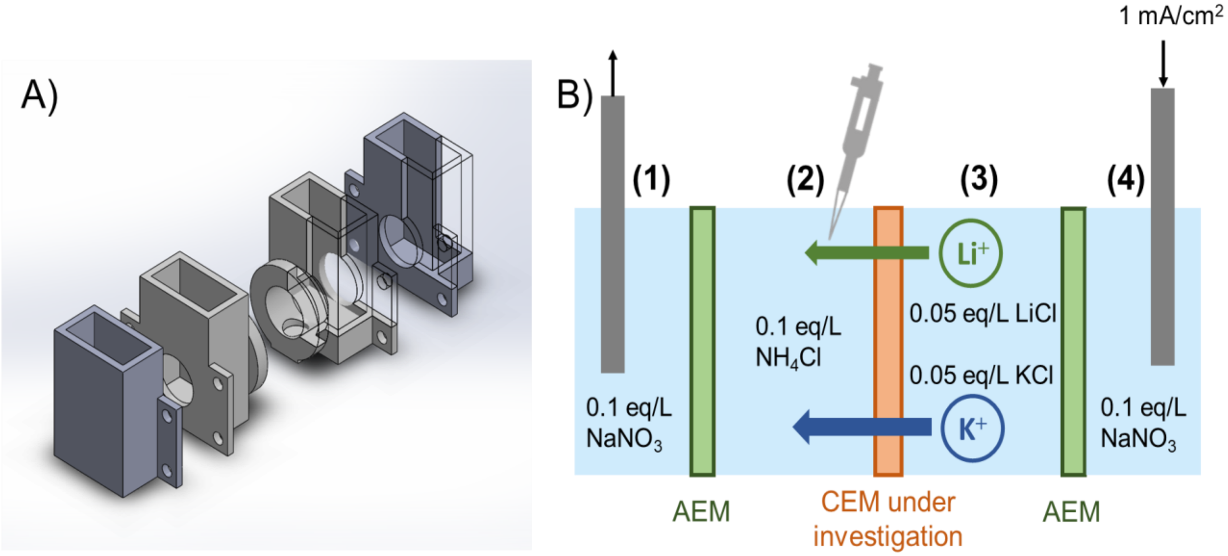

Figure S3: (A) Computer-aided design schematic of the 3D-printed four-chamber electrodialysis cell. (B) Schematic of the electrodialysis setup to characterize counterion transport selectivity.

RESULTS AND DISCUSSION

Section S4: Water content of fabricated membranes

The experimentally determined λ may slightly underestimate the actual water environment in the membrane matrix, because some water might remain tightly bound to the charged polymer even after the drying process in *SD* characterization.[2,3] Hence, the numerical values of the hydration analysis (e.g., 11.2 and 8.6 for Li^+ and K^+, respectively, in the main manuscript) should be taken as nominal. Additionally, water in the membrane may be hydrating other moieties besides the counterions and fixed charges, such as hydrophilic groups of the polymer backbone and trace concentrations of co-ions. Nevertheless, these uncertainties are relatively minor and do not change the overall conclusions.

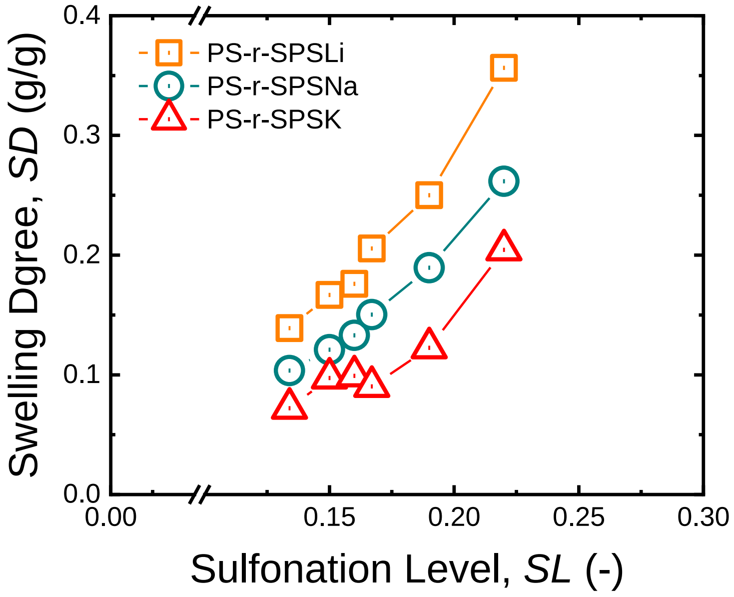

Figure S4: Swelling degree, *SD*, as a function of sulfonation level, *SL*, for PS-r-SPSLi, Na, and K membranes (orange square, green circle, and red triangle symbols, respectively).

Section S5: Ion selectivity data

Table S1: Ion concentrations in the receiver solution at different operation durations of the K$^+$/Li$^+$ transport selectivity experiments (Eqs. 8 and 9 of the main manuscript). Each concentration is the mean of duplicate samples analyzed by ion chromatography.

Water per fixed charge, λ (-)	**K$^+$ concentration ($\times 10^{-3}$ mol L^{-1})**			**Li$^+$ concentration ($\times 10^{-3}$ mol L^{-1})**			**K$^+$/Li$^+$ transport selectivity (-)**
	30 min	60 min		30 min	60 min		
6.28	4.94	10.02		1.58	3.29		3.08±0.05
7.88	5.59	11.12		1.82	3.71		3.04±0.06
8.79	6.56	12.78		2.22	4.47		2.91±0.07
	15 min	30 min	45 min	15 min	30 min	45 min	
8.87	1.94	3.81	5.81	0.65	1.25	1.92	3.02±0.03
9.59	2.97	5.72	8.58	1.02	2.01	3.08	2.84±0.05
12.20	4.55	8.43	12.18	1.79	3.44	5.15	2.45±0.09

Table S2: Ion concentrations in the eluent of the K$^+$/Li$^+$ sorption selectivity characterization (Eq. 10 in the main manuscript).

Water per fixed charge, λ (-)	**K$^+$ concentration ($\times 10^{-3}$ mol L^{-1})**	**Li$^+$ concentration ($\times 10^{-3}$ mol L^{-1})**	**K$^+$/Li$^+$ sorption selectivity (-)**
6.28	4.94	2.44	2.03
7.88	10.58	5.45	1.94
8.79	10.12	5.25	1.93
8.87	5.89	3.07	1.92
9.59	10.22	5.43	1.88
12.20	12.76	7.04	1.81

Section S6: Ion mobility, transport number, and bulk solution transport selectivity

Ion electrical mobility, u, and diffusion coefficient, D, are related by the expression[4]

$$u = \frac{|z|F}{RT} D \tag{S3}$$

where z is ion valence, F is the Faraday constant, R is the ideal gas constant, and T is absolute temperature. When electromigration is the dominant transport mechanism, i.e., diffusion due to ion concentration gradient is negligible, the Nernst-Planck equation for ion flux in the bulk solution and IEM matrix, J, simplifies to[4,5]

$$J = -\frac{DFzc}{RT}\frac{d\varphi}{dx} \tag{S4}$$

where c is ion concentration and $d\varphi/dx$ is the electric potential gradient. The transport number of ion i is defined as[5,6]

$$t_i = \frac{z_i J_i}{\sum_k z_k J_k} \tag{S5}$$

where the denominator is the summation across all ions. The transport selectivity, $S_{i/j}$, between two ionic species i and j in the bulk solution is[7,8]

$$S_{i/j} = \frac{t_i^{\mathrm{s}} / t_j^{\mathrm{s}}}{|z_i| c_i^{\mathrm{s}} / |z_j| c_j^{\mathrm{s}}} \tag{S6}$$

where superscript s denotes bulk solution phase. Essentially, $S_{i/j}$ is the ratio of transport numbers normalized by the ratio of equivalent ion concentrations in the solution. Substituting Eqs. S3-5 into S6 yields

$$S_{i/j} = \frac{u_i^{\mathrm{s}}}{u_j^{\mathrm{s}}} \tag{S7}$$

The electrical mobilities K^+ and Li^+ in bulk solution are 7.62×10^{-8} and 4.01×10^{-8} $m^2\ s^{-1} V^{-1}$, respectively.[9] Therefore, the K^+/Li^+ transport selectivity in bulk solution is 1.9, as presented in Figure 3 of the main manuscript.

Section S7: Influence of diffusive ion transport on experimental selectivity characterization

Ion flux in IEMs, J^{m}, can be described by the Nernst-Planck equation[5]

$$J^{\mathrm{m}} = -D^{\mathrm{m}} \frac{dc^{\mathrm{m}}}{dx} - \frac{D^{\mathrm{m}} F z c^{\mathrm{m}}}{RT} \frac{d\varphi^{\mathrm{m}}}{dx} \tag{S8}$$

where superscript m denotes membrane phase. The first and second terms in Eq. S8 represent diffusion driven by ion concentration gradient and electromigration under the electric field, respectively. The expression relating ion sorption selectivity, mobility selectivity, and transport selectivity, $S_{i/j} = K_{i/j} \times u_{i/j}$ (Eq. 11 of the main manuscript), implicitly assumes electromigration to be the dominant transport mechanism and diffusion is relatively small, i.e., can be neglected.[10] Although diffusive fluxes are not completely eliminated in the electrodialysis characterizations for ion transport selectivity (dc^{m}/dx for K^+ and Li^+ are nonzero), adequately large external electric potentials were rationally chosen for the experiments such that the driving force for electromigration is the dominant transport mechanism over ion diffusion. Therefore, $S_{i/j} \approx K_{i/j} \times u_{i/j}$ is generally valid.

Section S8: Ion-exchange capacity analysis

The *IEC* determined using sulfonation level, *SL*, from ^{1}H-NMR results, IEC_{NMR}, is calculated using

$$IEC_{\mathrm{NMR}} = \frac{SL}{(1-SL)MW_{\mathrm{PS}} + SL\,MW_{\mathrm{SPSM}}} \tag{S9}$$

where MW_{PS} is the molar mass of repeating styrene unit (104 g mol^{-1}), and MW_{SPSM} is the molar mass of sulfonated styrene unit neutralized by cation M (M = Li, Na, or K).

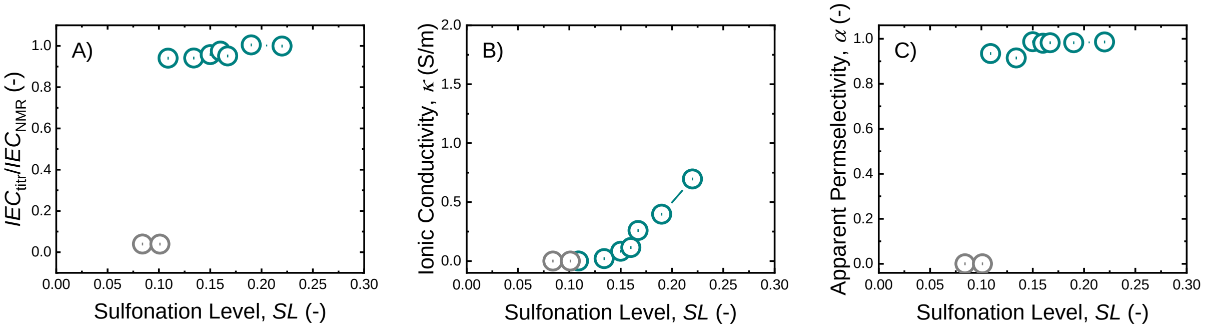

Figure S5: (A) Ion-exchange capacity characterized using the titration method, IEC_{titr}, normalized by the value determined using ^{1}H-NMR, IEC_{NMR}, (B) membrane ionic conductivity, *κ*, and (C) apparent permselectivity, *α*, as a function of sulfonation level for PS-r-SPSNa membranes. Gray symbols denote membranes with negligible IEC_{titr}.

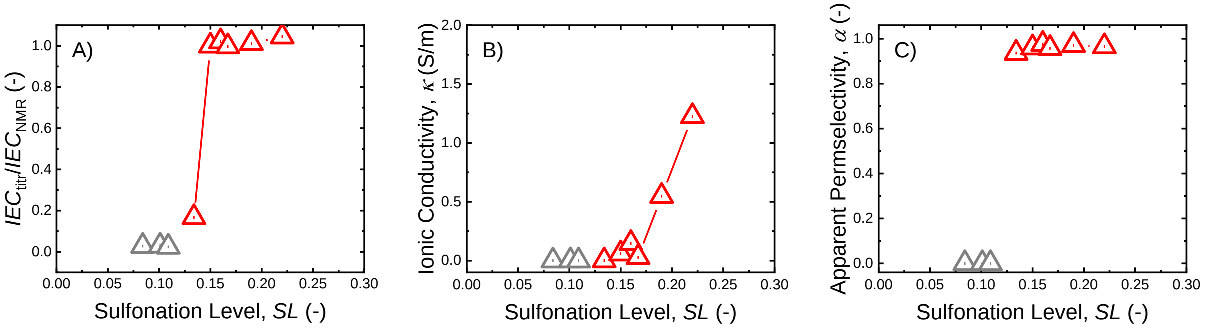

Figure S6: (A) Ion-exchange capacity characterized using the titration method, IEC_{titr}, normalized by the value determined using ^{1}H-NMR, IEC_{NMR}, (B) membrane ionic conductivity, *κ*, and (C) apparent permselectivity, *α*, as a function of sulfonation level for PS-r-SPSK membranes. Gray symbols denote membranes with negligible IEC_{titr}.

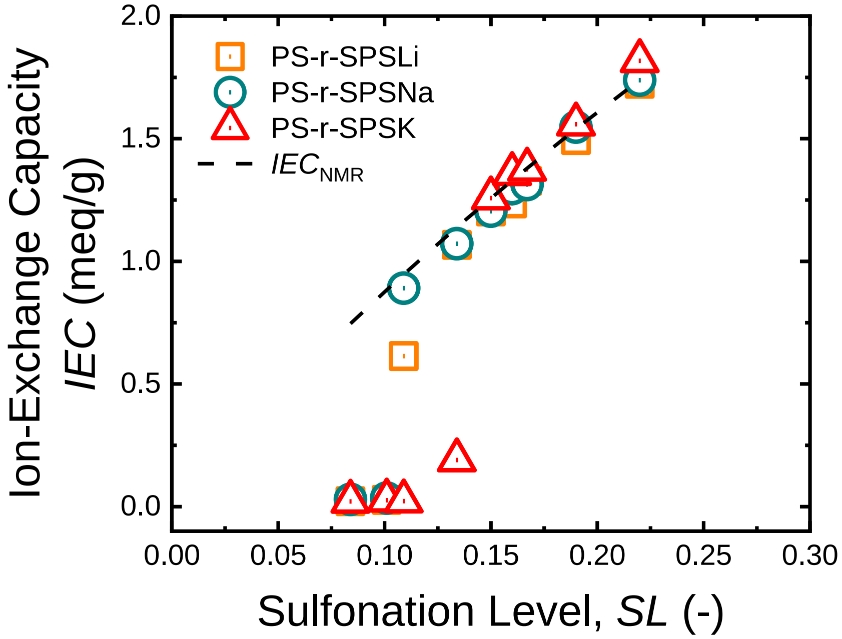

Figure S7: Ion-exchange capacity, *IEC*, as a function of sulfonation level, *SL*, for PS-r-SPSLi, Na, and K membranes (orange square, green circle, and red triangle symbols, respectively) characterized by acid-base titration (Eq. 1 of the main manuscript). Black dashed line is the *IEC* for PS-r-SPSNa calculated using *SL* determined using ^{1}H-NMR (Eq. S9).

Section S9: Conductivity and permselectivity

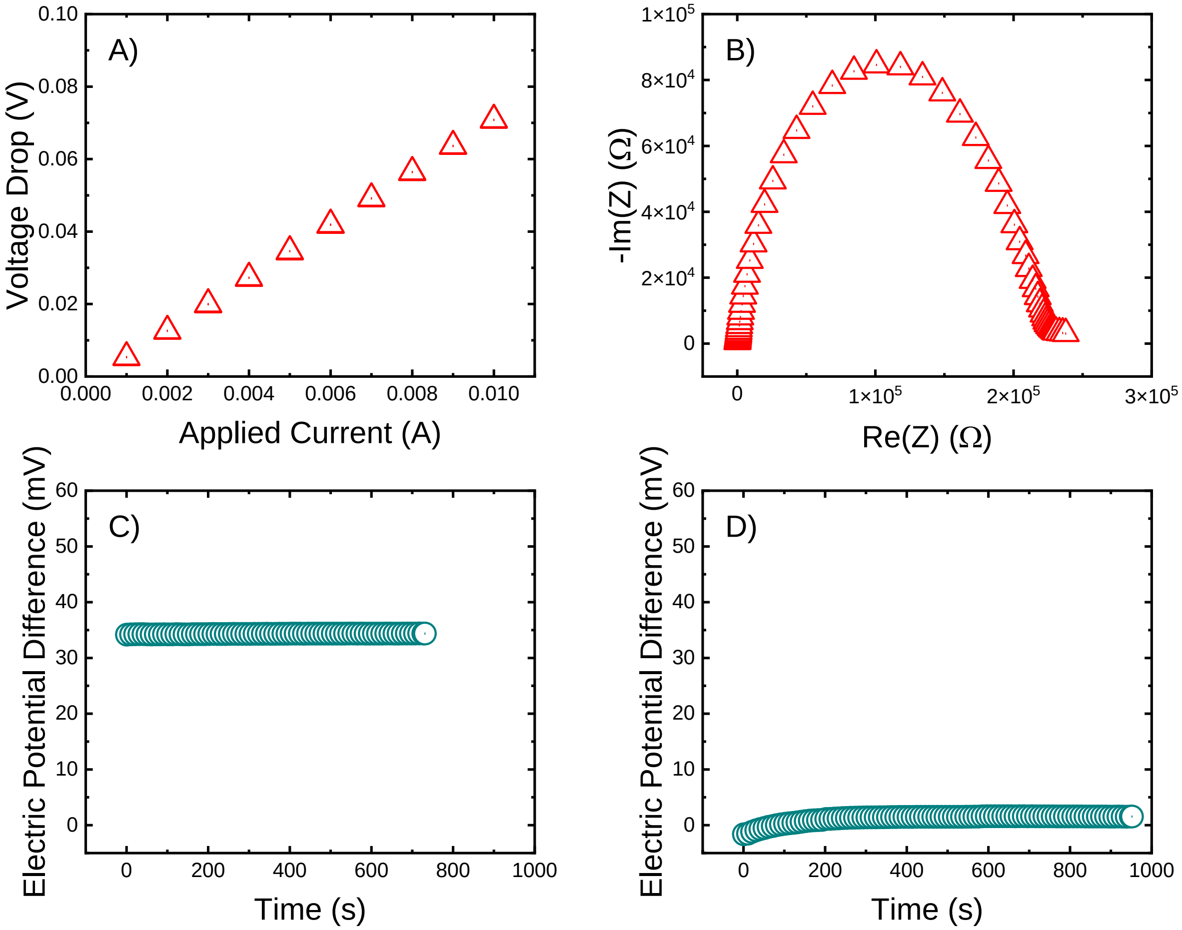

Figure S8: (A) Representative plot of voltage drop as a function of applied current for ionic conductivity analysis of functional membranes. The IEM is a PS-r-SPSK membrane with *SL* = 0.19 in 1.0 mol L^{-1} KCl solution. (B) Representative plot of imaginary impedance, -Im(Z), as a function of real impedance, Re(Z), i.e., Nyquist plot, for electrochemical impedance spectroscopy analysis of membranes with very high ionic resistance. The IEM is a PS-r-SPSK membrane with *SL* = 0.109 in 1.0 mol L^{-1} KCl solution. Representative plots of transmembrane electric potential difference as a function of time for (C) PS-r-SPSNa with *SL* = 0.19 and (D) PS-r-SPSNa with *SL* = 0.101 in permselectivity characterizations of functional and non-functional membranes, respectively. The membranes are separating 0.50 and 0.10 mol L^{-1} NaCl solutions.

Section S10: Wide-angle X-ray scattering (WAXS) analysis

As discussed in the main manuscript, the micro- and nanostructure of the PS-r-SPS random copolymer membranes were characterized using a laboratory wide-angle X-ray scattering (WAXS) system with a Cu Kα source, Pilatus 300k detector, and a variable sample-to-detector distance. Two separate sample-to-detector distances, 180.2 mm, and 521.4 mm, were used to collect scattering data with optimal signal-to-noise from $0.16 < q < 17$ nm^{-1}. 2D scattering images (.tiff) were averaged over 300 s (180.24 mm) and 600 s (521.44 mm). Pixels corresponding to the beam-stop and malfunctioning regions were subtracted from the .tiff images using the pyFAI package with the AzimuthalIntegrator class and associated methods.[11] Error in the scattering data was estimated using the variance along the azimuthal angle. Data from the two separate sample-to-detector distances were stitched together at $q = 1.4$ nm^{-1} based on the normalized scattering intensity in the nearest five-point range.

Figure S9A shows a representative X-ray scattering spectrum for a dry, neutralized PS-r-SPSNa copolymer. During the solvent casting and subsequent annealing steps, the disparate polarity between SPS and PS drives the formation of clusters of SPS monomers and their neutralizing counterions.[12,13] It is generally accepted that scattering *between* clusters produces the ionomer peak at $q \approx 2$ nm^{-1} in Figure S9A.[14,15]

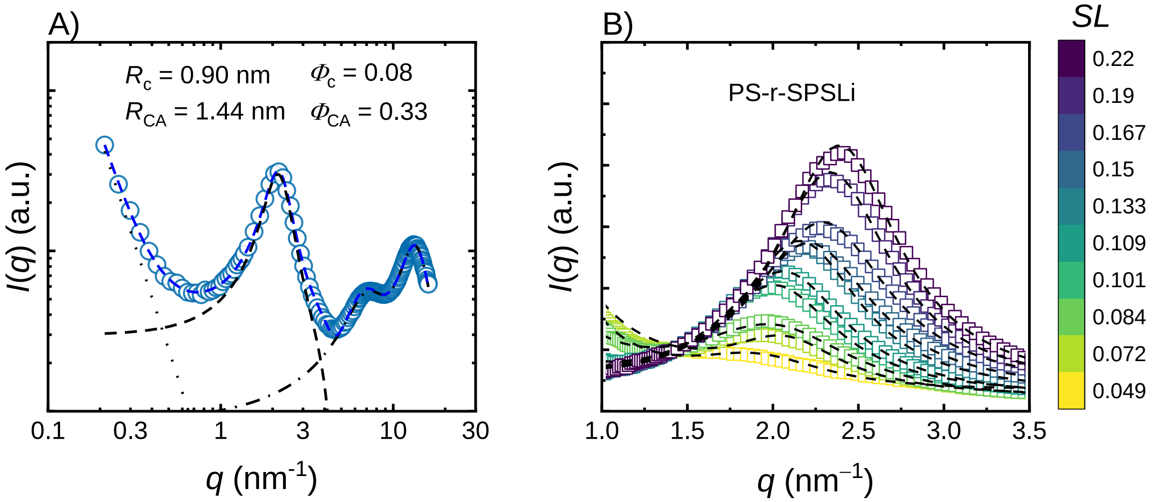

Figure S9: (A) A representative wide-angle X-ray scattering (WAXS) spectrum of neutralized PS-r-SPSNa membranes with $SL = 0.19$. Power-law, Lorentzian, and ionomer fits (dotted, dash-dotted, and dashed lines, respectively) are summed in the overall model (blue dashed line). Fitted radii, R, and volume fractions, ϕ, of the ion clusters and Percus-Yevick hard-spheres (denoted by subscripts c and CA, respectively) are indicated. (B) Normalized WAXS spectra for PS-r-SPSLi membranes with SL between 0.05 and 0.22. Dashed lines signify the model fittings (Eq. S10).

In order to isolate and model the scattering arising from the ion clusters for each neutralized copolymer, the additional scattering features first need to be accounted for. At high scattering angles, there are two peaks that correspond to the highly local structure of the polymer glass. The polymerization peak at $q \approx 7$ nm^{-1} results from correlations between monomers on the polymer chain, and the amorphous halo at $q \approx 13$ nm^{-1} corresponds to the highly local, amorphous structure of the polymer.[16,17] Both peaks are present in polystyrene prior to sulfonation, and are accounted for using Lorentzians $I_{\mathrm{Lor}}^{\mathrm{poly}}$ and $I_{\mathrm{Lor}}^{\mathrm{AH}}$ (black dash-dotted line in Figure S9A). At low-q, an exponential increase in the scattering intensity is attributed to nonhomogeneous distributions of ions with large correlation lengths, which is accounted for using a power-law expression with exponent $m \approx 3$ and front coefficient A (black dotted line).[18,19] This allows the isolation of the scattering from the ionomer peak, which is modeled using a Percus-Yevick hard-sphere structure factor (PY-HS, black dashed line), a slight modification of the model proposed by Yarusso and Cooper.[20–22] Parenthetically, we note that past studies have found good agreement between the results of the Yarusso-Cooper model with high-angle annular dark-field transmission electron microscopy (HAADF-TEM) images after accounting for the finite thickness of the microtomed samples.[23–25]

The overall expression is shown below, with the four terms on the right-hand side representing the nonhomogeneous distributions of ions, the ionomer peak, the polymerization peak, and the amorphous polymer structure peak, respectively:

$$I\left(q\right) = Aq^{-\mathrm{m}} + \left(\Delta\eta\right)^2 \phi_{\mathrm{c}} v_{\mathrm{c}} F\left(qR_{\mathrm{c}}\right) S^{\mathrm{PY}}\left(q, \phi_{\mathrm{c}}, R_{\mathrm{CA}}\right) + I_{\mathrm{Lor}}^{\mathrm{poly}} + I_{\mathrm{Lor}}^{\mathrm{AH}} \tag{S10}$$

where $\Delta\eta$ is the scattering length density difference (reflects the electronic density difference between the clusters and the surrounding PS-rich matrix), $F(qR_{\mathrm{c}})$ is the analytical form factor for scattering from monodisperse spheres of radius R_{c}, and $S^{\mathrm{PY}}(q, \phi_{\mathrm{c}}, R_{\mathrm{CA}})$ is the PY-HS structure factor for hard-spheres with radii R_{CA} (Figure S10) and volume fraction ϕ_{CA}. The sulfonated monomers form clusters with a characteristic radius, R_{c} (Figure S10), volume, v_{c}, and volume fraction, ϕ_c. In the absence of interactions from adjacent, spherical clusters (i.e., in the dilute limit), scattering from these spheres is described by a monodisperse, spherical form factor, $F(qR_c)$. Correlations between spheres are described by the PY-HS structure factor, which is an analytical closure to the Ornstein-Zernike equation. The PY-HS only requires two parameters: the hard-sphere radius R_{CA}, which dictates the separation between neighboring, spherical clusters, and the hard-sphere volume fraction, $\phi_{CA} = v_c(R_{CA}/R_c)^3$, which determines the height of the peak and its behavior in the limit of low-q. Thus, after separately regressing parameters for the Lorentzian functions ($I_{\mathrm{Lor}}^{\mathrm{poly}}$ and $I_{\mathrm{Lor}}^{\mathrm{AH}}$) and the power-law scattering (Aq^{-m}), the ionomer peak is modeled using only four adjustable parameters: $\Delta\eta$, R_c, R_{CA}, and v_c. The final parameter ($\Delta\eta$) vertically scales the data, has no q-dependence, and reflects the electronic density difference between the clusters and the surrounding PS-rich matrix. The blue dashed line in Figure S9A illustrates an example fit. In order to probe the correlation between the four adjustable parameters and uncertainty distributions in the ion cluster model, $\Delta\eta$, R_c, R_{CA}, and v_c, the *bumps* python package was used. Representative glove curve-fitting results are shown below in Figure S11.

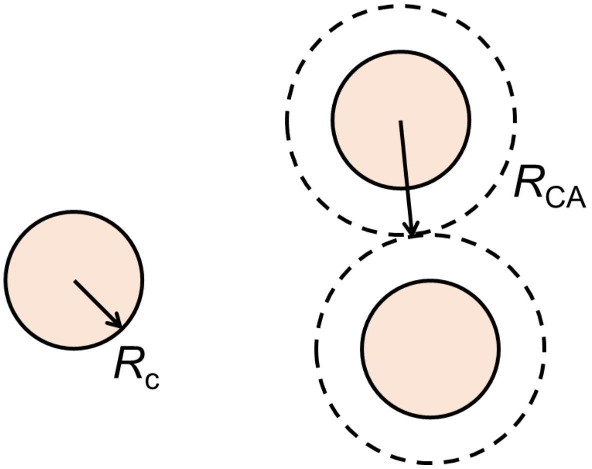

Figure S10: Schematic illustrating the ion cluster radius, R_c, and the half distance of the closest approach between ion clusters, R_{CA}, i.e., the hard sphere radius in the PY-HS structure factor.

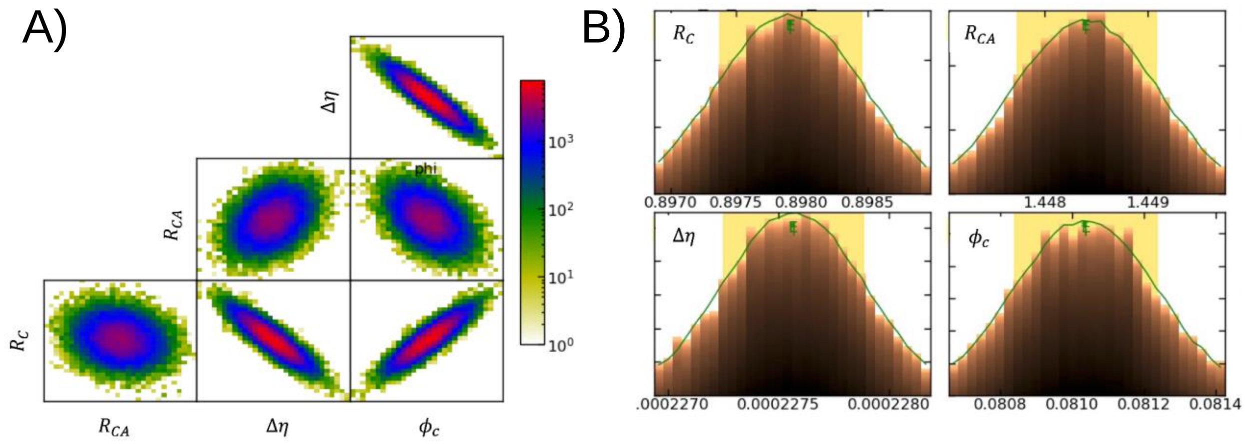

Figure S11: Representative global curve-fitting results[26] for WAXS spectra presented in Figure 5 of the main manuscript. (A) Correlations between parameters, where circular heat-maps suggest ideal decoupling of model parameters. (B) Histogram of model-fit parameter values with indicated expected value (labeled by "E") and best-fit value (vertical green lines). Shaded 68% confidence intervals were used to estimate uncertainty in best-fit parameters.

The analytical procedure was applied to the dry PS-r-SPS copolymers with the three different neutralizing cations (Li, Na, and K) and sulfonation levels between 0.05 and 0.22. The scattering data of PS-r-SPSLi across the *SL* range, normalized at $q = 1.4\ \text{nm}^{-1}$, is shown in Figure S9B (black dashed lines indicate model fittings). WAXS spectra and fittings for PS-r-SPSNa and PS-r-SPSK are displayed in Figures S12A and S12B, respectively. Two qualitative features can be immediately identified. Firstly, as more sulfonate groups are added to the copolymer, the relative contribution of the ionomer peak increases. Secondly, the average *d*-spacing, i.e., $2\pi/q_{\text{max}}$ decreases.

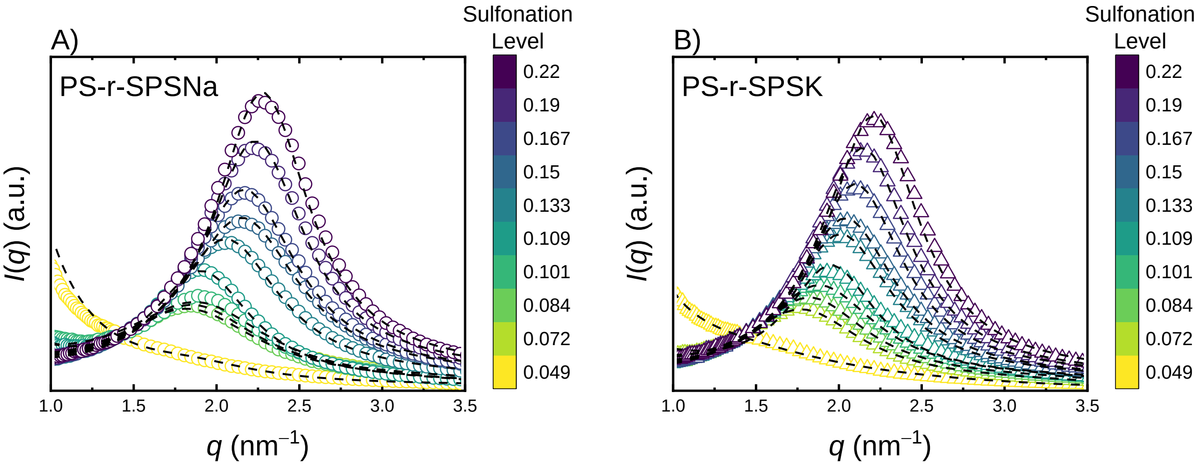

Figure S12: Normalized WAXS spectra for (A) PS-r-SPSNa and (B) PS-r-SPSK membranes with *SL* ranging from 0.049 to 0.22.

Section S11: Membrane conductivity trend analysis

As discussed in the main manuscript, the fitted κ_0s are 8.5, 19.3, and 39.3 S m^{-1} for PS-r-SPSLi, Na, and K membranes, respectively. This trend is attributed to the difference in mobility and concentration of counterions within the membrane. As ion mobility within the membrane is proportional to the mobility in bulk solution phase,[27,28] which ranks $Li^+ < Na^+ < K^+$, the orderings of κ_0 and κ are, thus, consistent with the bulk ion diffusion coefficients (Einstein relation). Additionally, because the membrane water content follows PS-r-SPSLi > PS-r-SPSNa > PS-r-SPSK (Figure S4), the fixed charge density of the IEMs neutralized by different counterions is ordered $Li^+ < Na^+ < K^+$, which is essentially the ranking of counterion concentration in the membrane (due to electroneutrality), i.e., PS-r-SPSK membranes have the highest concentration of mobile charge carriers whereas PS-r-SPSLi membranes have the lowest density, contributing to the κ_0 and κ trends.

REFERENCES

(1) Seo, J.; Kushner, D. I.; Hickner, M. A. 3D Printing of Micropatterned Anion Exchange Membranes. *ACS Appl. Mater. Interfaces* **2016**, *8* (26), 16656–16663. https://doi.org/10.1021/acsami.6b03455.

(2) Díaz, J. C.; Park, J.; Shapiro, A.; Patel, H.; Santiago-Pagán, L.; Kitto, D.; Kamcev, J. Understanding Monovalent Cation Diffusion in Negatively Charged Membranes and the Role of Membrane Water Content. *Macromolecules* **2024**, *57* (5), 2468–2481. https://doi.org/10.1021/acs.macromol.3c02655.

(3) Tran, T.; Lin, C.; Chaurasia, S.; Lin, H. Elucidating the Relationship between States of Water and Ion Transport Properties in Hydrated Polymers. *J. Membr. Sci.* **2019**, *574*, 299–308. https://doi.org/10.1016/j.memsci.2018.12.059.

(4) Bard, A. J.; Faulkner, L. R.; White, H. S. *Electrochemical Methods: Fundamentals and Applications*; John Wiley & Sons, 2022.

(5) Strathmann, H. *Ion-Exchange Membrane Separation Processes*; Elsevier, 2004.

(6) Sata, T. *Ion Exchange Membranes: Preparation, Characterization, Modification and Application*; Royal Society of chemistry, 2007.

(7) Sata, T.; Sata, T.; Yang, W. Studies on Cation-Exchange Membranes Having Permselectivity between Cations in Electrodialysis. *J. Membr. Sci.* **2002**, *206* (1–2), 31–60.

(8) Sata, T. Studies on Anion Exchange Membranes Having Permselectivity for Specific Anions in Electrodialysis—Effect of Hydrophilicity of Anion Exchange Membranes on Permselectivity of Anions. *J. Membr. Sci.* **2000**, *167* (1), 1–31.

(9) Luo, T.; Abdu, S.; Wessling, M. Selectivity of Ion Exchange Membranes: A Review. *J. Membr. Sci.* **2018**, *555*, 429–454.

(10) Fan, H.; Huang, Y.; Yip, N. Y. Advancing Ion-Exchange Membranes to Ion-Selective Membranes: Principles, Status, and Opportunities. *Front. Environ. Sci. Eng.* **2023**, *17* (2), 25.

(11) Ashiotis, G.; Deschildre, A.; Nawaz, Z.; Wright, J. P.; Karkoulis, D.; Picca, F. E.; Kieffer, J. The Fast Azimuthal Integration Python Library: pyFAI. *J. Appl. Crystallogr.* **2015**, *48* (2), 510–519.

(12) Galambos, A.; Stockton, W.; Koberstein, J.; Sen, A.; Weiss, R.; Russell, T. Observation of Cluster Formation in an Ionomer. *Macromolecules* **1987**, *20* (12), 3091–3094.

(13) Eisenberg, A. Clustering of Ions in Organic Polymers. A Theoretical Approach. *Macromolecules* **1970**, *3* (2), 147–154.

(14) Eisenberg, A.; Hird, B.; Moore, R. A New Multiplet-Cluster Model for the Morphology of Random Ionomers. *Macromolecules* **1990**, *23* (18), 4098–4107.

(15) Moore, R. B.; Bittencourt, D.; Gauthier, M.; Williams, C. E.; Eisenberg, A. Small-Angle X-Ray Scattering Investigations of Ionomers with Variable-Length Side Chains. *Macromolecules* **1991**, *24* (6), 1376–1382.

(16) Castagna, A. M.; Wang, W.; Winey, K. I.; Runt, J. Influence of the Degree of Sulfonation on the Structure and Dynamics of Sulfonated Polystyrene Copolymers. *Macromolecules* **2010**, *43* (24), 10498–10504.

(17) Castagna, A. M.; Wang, W.; Winey, K. I.; Runt, J. Influence of Cation Type on Structure and Dynamics in Sulfonated Polystyrene Ionomers. *Macromolecules* **2011**, *44* (13), 5420–5426.

(18) Ding, Y. S.; Hubbard, S. R.; Hodgson, K. O.; Register, R. A.; Cooper, S. L. Anomalous Small-Angle X-Ray Scattering from a Sulfonated Polystyrene Ionomer. *Macromolecules* **1988**, *21* (6), 1698–1703.

(19) Chu, B.; Wu, D. Q.; Lundberg, R. D.; MacKnight, W. J. Small-Angle X-Ray Scattering (SAXS) Studies of Sulfonated Polystyrene Ionomers. 1. Anomalous SAXS. *Macromolecules* **1993**, *26* (5), 994–999.

(20) Biehl, R. Jscatter, a Program for Evaluation and Analysis of Experimental Data. *PLoS One* **2019**, *14* (6), e0218789.

(21) Yarusso, D. J.; Cooper, S. L. Microstructure of Ionomers: Interpretation of Small-Angle x-Ray Scattering Data. *Macromolecules* **1983**, *16* (12), 1871–1880.

(22) Yarusso, D.; Cooper, S. L. Analysis of SAXS Data from Ionomer Systems. *Polymer* **1985**, *26* (3), 371–378.

(23) Benetatos, N. M.; Smith, B. W.; Heiney, P. A.; Winey, K. I. Toward Reconciling STEM and SAXS Data from Ionomers by Investigating Gold Nanoparticles. *Macromolecules* **2005**, *38* (22), 9251–9257.

(24) Benetatos, N. M.; Heiney, P. A.; Winey, K. I. Reconciling STEM and X-Ray Scattering Data from a Poly (Styrene-r an-Methacrylic Acid) Ionomer: Ionic Aggregate Size. *Macromolecules* **2006**, *39* (16), 5174–5176.

(25) Benetatos, N. M.; Chan, C. D.; Winey, K. I. Quantitative Morphology Study of Cu-Neutralized Poly (Styrene-Ran-Methacrylic Acid) Ionomers: STEM Imaging, X-Ray Scattering, and Real-Space Structural Modeling. *Macromolecules* **2007**, *40* (4), 1081–1088.

(26) Kienzle, P. Bumps: Curve Fitting and Uncertainty Analysis. **2018**.

(27) Mackie, J.; Meares, P. The Diffusion of Electrolytes in a Cation-Exchange Resin Membrane I. Theoretical. *Proc. R. Soc. Lond. Ser. Math. Phys. Sci.* **1955**, *232* (1191), 498–509.

(28) Jannasch, P.; Weiber, E. A. Configuring Anion-exchange Membranes for High Conductivity and Alkaline Stability by Using Cationic Polymers with Tailored Side Chains. *Macromol. Chem. Phys.* **2016**, *217* (10), 1108–1118.